remote sensing

MDPI

Article

Hyperspectral Investigation of an Abandoned Waste Mining Site: The Case of Sidi Bou Azzouz (Morocco)

Daniela Guglietta [1,†], Roberto Salzano [2,*,†], Amina Wafik [3], Aida M. Conte [1], Matteo Paciucci [1], Rosalda Punturo [1,4], Rosamaria Salvatori [5], Giorgio S. Senesi [6] and Carmela Vaccaro [7]

[1] Institute of Environmental Geology and Geoengineering, National Research Council, Via Salaria km 29,300, 00015 Rome, Italy; daniela.guglietta@cnr.it (D.G.); aidamaria.conte@cnr.it (A.M.C.); matteo.paciucci@cnr.it (M.P.); punturo@unict.it (R.P.)
[2] Institute of Atmospheric Pollution Research, National Research Council, Via Madonna del Piano, 10, 50019 Florence, Italy
[3] AQUABIOTECH Laboratory, Department of Geology, Faculty of Sciences Semlalia, Cadi Ayyad University, Bd Prince Moulay Abdellah, Marrakech 400000, Morocco; wafik@uca.ac.ma
[4] Department of Biological Geological and Environmental Sciences, Università degli Studi di Catania, Corso Italia, 59, 95129 Catania, Italy
[5] Institute of Polar Sciences, National Research Council, Via Salaria km 29,300, 00015 Rome, Italy; rosamaria.salvatori@cnr.it
[6] Institute for Plasma Science and Technology, National Research Council, Via Amendola 122/D, 70126 Bari, Italy; giorgiosaverio.senesi@cnr.it
[7] Department of Environmental Sciences and Prevention, Università degli Studi di Ferrara, Via Giuseppe Saragat, 1, 44122 Ferrara, Italy; vcr@unife.it
* Correspondence: roberto.salzano@cnr.it
† These authors contributed equally to this work.

Abstract: The increasing demand for critical raw materials (CRMs), driven by global energy transition, underscores the need for innovative approaches to identify secondary resources, such as mining residues. Mining residues, often overlooked during initial mining activities, now represent valuable sources of raw materials thanks to technological advancements, including hyperspectral remote sensing. This study investigates the potential of hyperspectral satellite imagery to detect and map CRMs in mining residues of the abandoned Sidi Bou Azzouz mine in Morocco. The proposed approach is based on the integration between satellite data, field spectroscopy, chemical, and mineralogical analyses in a strong multi-scale and interdisciplinary framework. The integration between advanced laboratory techniques, including LIBS, XRF, XRPD, and SEM-EDS, was employed to enhance hyperspectral data interpretation. The integration of remote sensing and laboratory results provided a comprehensive understanding of mineral composition, confirming the effectiveness of hyperspectral methods for characterizing heterogeneous surface deposits. This research demonstrates the potential of hyperspectral observations to identify valuable raw materials and to map them using PRISMA imagery in abandoned mining residues, offering a tool useful for planning cost-effective and sustainable solutions aimed at answering the growing demand for CRMs crucial to industrial competitiveness and sustainable growth.

Keywords: hyperspectral remote sensing; critical raw materials; spectral mineralogy; geochemistry; diffractometry; spectroscopy

Academic Editors: Hai Li and Zhenwei Guo

Received: 4 April 2025
Revised: 17 May 2025
Accepted: 22 May 2025
Published: 24 May 2025

Citation: Guglietta, D.; Salzano, R.; Wafik, A.; Conte, A.M.; Paciucci, M.; Punturo, R.; Salvatori, R.; Senesi, G.S.; Vaccaro, C. Hyperspectral Investigation of an Abandoned Waste Mining Site: The Case of Sidi Bou Azzouz (Morocco). *Remote Sens.* **2025**, *17*, 1838. https://doi.org/10.3390/rs17111838

1. Introduction

Since the 1970s, Earth Observation data have been used in the mining sector to map the distribution of different lithologies, to explore new sites, and to monitor environmental critical issues. Recently, remote sensing by various satellite and airborne platforms, multi and hyperspectral, has been increasingly applied in the characterization of several material deposit types in active and abandoned mines [1–5]. In particular, the availability of open-access satellite imagery with higher spectral and spatial resolutions makes remote sensing techniques even more exploitable in all phases of mining activities. Typical spectral features in different regions of the electromagnetic spectrum (reflectance spectroscopy) have also been applied to characterize and identify the mineralogy and speciation of critical raw materials in a rapid and cost-effective manner [3,6]. In recent years, raw materials have become increasingly crucial and indispensable for ecological transition, industrial competitiveness, and the health and safety of citizens [7]. Recently, uncertainty in the supply of raw materials to global production networks has pushed private and non-corporate actors such as the European Union (EU) and the United Nations (UN) to act in the global race to detect and extract critical raw materials. Because of this, action plans and initiatives improving circularity and sustainability began to strengthen the resilience and strategic autonomy that depend on the availability of raw materials [8,9]. The UN Secretary-General's Panel on Critical Energy Transition Minerals highlights the need to reconcile the acceleration of mineral extraction for energy transition requirements with the well-being of countries and local communities that have these resources and addresses issues of equity, transparency, investment, sustainability, and human rights. The Working Group on Extractive Industries Transformation for Sustainable Development, in its flagship initiative "Harnessing Critical Minerals of the Energy Transition for Sustainable Development", highlights the need to census and protect critical raw material deposits to facilitate sustainable measures and critical raw material value chains in global production networks.

The raw material demand is expected to increase in the future, and the development of new strategies is currently needed to meet the expectations of strategic sectors and technologies [7,10–12]. Earth Observation can help address the growing demand for critical minerals for production systems towards a sustainable energy transition [1,13,14]. In recent years, historic mining sites with abandoned stockpiles have attracted scientific interest because they potentially contain minerals of economic importance. Such deposits represent novel resources since original strategies for the industry were not targeted at the time of the initial mining activity [15].

Hyperspectral imaging systems, with high spectral resolutions, are valuable tools for the accurate characterization of key pathfinder minerals [16–18] and for distinguishing between mining residues according to extraction and mineral resource processing, such as in overburden, waste rock, mine spoils, and tailings [19–22]. The classification of raw materials depends on attributes such as grain size, residual economic value, and potential risk after storage [23]. These novel sensors are nowadays available in situ, airborne even on unmanned vehicles, and onboard on spacecrafts. Referring to spaceborne platforms, hyperspectral sensors are included in several satellite missions (Italy's PRISMA, Germany's EnMap, China's GF-5, USA's EMIT, and Japan's HISUI), which are under investigation for mining purposes [20–22,24]. Particular attention of the community is focused on the Hyperspectral Precursor of the Application Mission (PRISMA) satellite, launched on 22 March 2019. The mission has been developed, owned, and operated by Agenzia Spaziale Italiana (ASI), and it is aimed at providing observations and data about land surface, agriculture and forestry, regional geology, land use studies, water resources, vegetation studies, coastal studies, and soils. The PRISMA hyperspectral platform carries VNIR-SWIR imaging spectrometers operating in the 400–2500 nm spectral range with 30 m spatial resolution and a high-resolution panchromatic camera (PAN), with 5 m spatial resolution [25]. The use of such data is a promising tool for exploiting mining activities [19], but further missions will be launched in the near future, significantly increasing the EO capabilities. Such novel sensors, together with additional geophysical technologies, positioning systems, autonomous trucks, and drones, will be the frontier for exploration and mining in the framework of Mining 4.0 [26].

Since a large amount of mining residues has been produced in recent decades worldwide, the lack of detailed data (i.e., exact positioning, chemical and mineralogical composition, and minerals yet to be exploited) about materials, considered below the cut-off grade at the time of initial mining activity, is a major gap. Currently, several national databases exist, but they only concern the period of mining activity; indeed, there are no data on where and how the residues were placed [23]. This information is now valuable because we want to use the residues with modern extraction techniques, improving recovery, remediation, and creating value chains of critical raw materials.

Nowadays, the development of advanced technologies enables us to fill data gaps concerning the distribution patterns of minerals in ore deposits and in the waste material of nearby areas. Novel approaches will support the reusing of mining residues as a potential source of raw materials. In this context, remote sensing and reflectance spectroscopy can play a fundamental role in exploiting the spectral characteristics of waste generated by the mining, processing, and disposal phases. These methods are less expensive, eco-friendly, and faster compared to traditional techniques used to identify minerals of interest in the valuable reserves of resources present in easily accessible mining residues [27].

The study area is part of the complex geological framework of the Rehamna region in central Morocco, where tectono-magmatic activity has led to the presence of hydrothermal fluids [28]. Significant Paleozoic and Permo-Carboniferous magmatism, particularly granite intrusions, occurred in the Rehamna Massif [29]. These magmatic bodies function as heat sources, heating groundwater and enabling them to interact with nearby rocks, thus driving the circulation of hydrothermal fluids [30]. The region is intersected by numerous faults and fractures, especially those trending NW–SE and NE–SW, which allow deeply seated fluids to move upward. These faults were reactivated during tectonic events, creating pathways for mineralization and fluid migration. Hydrothermal fluids in Rehamna were also enriched by regional metamorphic processes and incompatible elements (W, Sn, and Cu above all), and other ore deposits [31]. When these fluids encountered variations in temperature, pressure, or chemical composition, they often precipitated minerals, forming veins and alteration halos. The Sidi Bou Azzouz mining site was closed due to a complex interplay of social challenges, environmental degradation, and economic pressures [32]. These factors collectively made it unfeasible to continue mining operations at the site, leading to its closure.

The main objective of this research is to evaluate the contribution of multi-source data integration regarding satellite hyperspectral imaging. Different spaceborne platforms are nowadays available, but, adding a stratified approach, we defined a multi-scale solution for the identification of spectral endmembers. Combining in situ ground truthing through field surveys, sampling, and laboratory analysis, we are presenting an intermediate level of knowledge between satellite data and field evidence. Particular attention was focused on selecting a small and abandoned mining site where stockpiles of mining waste and tailings differentiate such an application from state-of-the-art regional studies, concerned with mineral exploration on lithologies. To achieve this, this study adopts an interdisciplinary approach that integrates the Laboratory VIS-NIR-SWIR spectroscopy (LS) of raw material samples with their petrographic, mineralogical, and chemical analyses and satellite hyperspectral imaging (HSI) of the sampling sites extracted from PRISMA images. The most advanced techniques, including Laser-Induced Breakdown Spectroscopy (LIBS), X-ray Fluorescence (XRF), X-ray Powder Diffraction (XRPD), and Scanning Electron Microscopy with Energy Dispersive X-ray Spectroscopy (SEM-EDS), were used to confirm the presence of minerals in the mining residues. As mining residues are increasingly recognized as potential sources of raw materials worldwide, these technologies can play a critical role in evaluating and exploiting such materials. The interdisciplinary methodology developed in this research aims to assess the feasibility of detecting valuable raw materials in the study area by leveraging the unique strengths of these analytical tools.

2. Study Site, Materials, and Methods

The multidisciplinary approach presented in this study is based on the geological framework of the region of interest, which serves as the foundation for defining the sampling strategy. Hyperspectral data, both obtained in the laboratory and acquired by a satellite platform, function as a gap-filling tool between the spatial distribution of mining residues and traditional geochemical and mineralogical techniques.

2.1. The Geological Framework of the Study Area

The Sidi Bou Azzouz closed and abandoned mine in the eastern Rehamna (Morocco) represents a significant geological and economic resource, having previously been exploited in the 1980s as a tungsten ore mine [33]. The tungsten deposits are hosted within a hydrothermal quartz vein system and continue to hold potential for future extraction. Studying them offers insight into the broader geological history of the Rehamna massif, located 90 km north of Marrakech within the western Meseta Domain. This massif is divided into septentrional and meridional sections and is characterized by distinct structural and metamorphic units [28]. In particular, the southern Rehamna region, where Sidi Bou Azzouz is situated, is categorized into three structural units related to the Variscan orogeny, namely, the western, central, and eastern Rehamna (Figure 1).

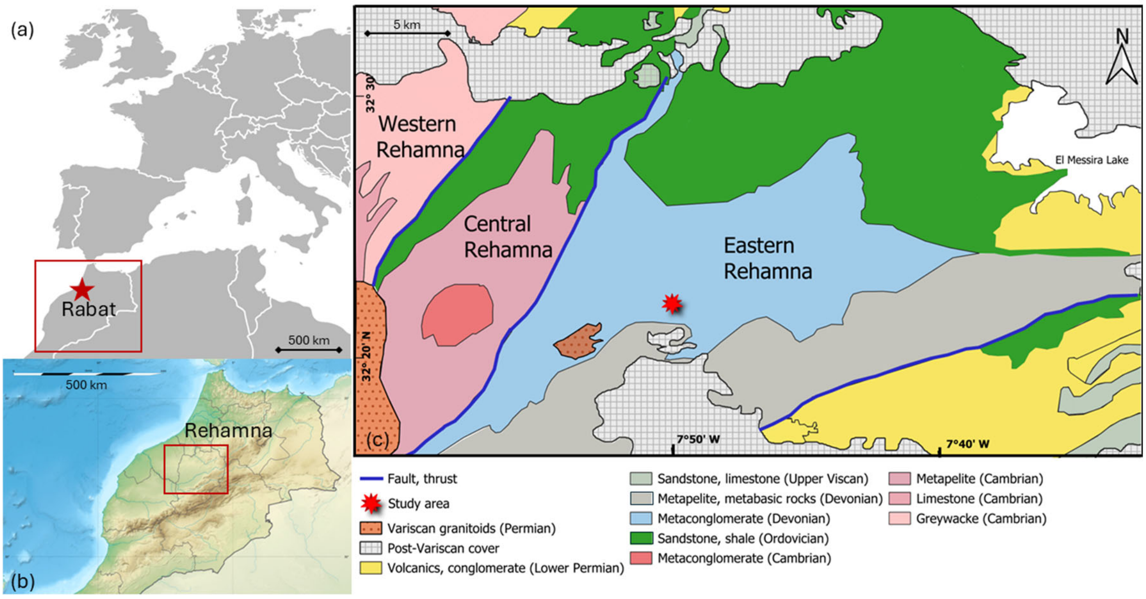

Figure 1. The location of the Sidi Bou Azzouz study area in the western Mediterranean area (**a**), in northern Morocco (**b**), and in a geological sketch of the Rehamna Massif (**c**), modified after [29].

The Massif also features lower Permian magmatic intrusions (Figure 1), such as the Ras el Abiod and Koudiat er Ramel granitoids, which are part of an expansive batholith impacting the Oulad Hassine and Lalla Tittaf formations [28,29]. This magmatism has influenced mineralization patterns, linking granitoids with mineralized veins that host tungsten, lead, lithium, beryllium, and other metals. Tungsten deposits are limited in extent and abundance, as they are generated by fluids in the magmatic–hydrothermal transition phases often associated with highly fractionated alkali-granites and fluid–rock interactions [30,31]. Tungsten precipitation is controlled by the availability of cations such as Fe, Mn, and Ca, which are necessary for the formation of W-bearing minerals such as wolframite and scheelite. These fluids of the magmatic–hydrothermal transition processes are therefore associated with rocks of alkaline–granite composition that are distinguished by the presence of muscovite, lepidolite, alkali feldspars, quartz, wolframite, and scheelite minerals that are characteristic spectral signatures or ore minerals fingerprints. Furthermore, hydrothermal fluids of magmatic origin transported through faults or other permeable structures can react with carbonate rocks (marbles), favoring the precipitation of scheelite ($CaWO_4$), for which W mineralization is associated with spectral signatures indicating high-calcium concentrations in the calcium-poor granite rocks.

In the eastern part of the Rehamna massif, where the study area is located, the metamorphic units belong to the Oulad Hassine Formation. These metamorphic units exhibit varied mineral assemblages and microstructural features. The greenschist facies rocks are characterized by fine-grained, dark gray-blue schists with quartz lenses and quartzite [34,35]. These rocks are rich in biotite and chlorite, indicating low-grade metamorphic conditions. The amphibolite facies rocks, which represent a higher metamorphic grade, are characterized by alternating layers of muscovite and biotite with late-stage chlorite, along with quartz boudins. Together, these facies reflect a complex metamorphic history influenced by various pressure and temperature conditions [28–31]. The Sidi Bou Azzouz abandoned mine sits on the metaconglomerate (Figure 1) and covers an area of about 920 km^2. The major deposits are in the smallest sector, which extends to approximately 0.3 km^2. This zone includes two major tunnels and one processing facility. The outcropping residues consist of materials with different extraction ages.

2.2. The Sampling Strategy

The study site was characterized by two different field surveys. During the first in situ campaign conducted in May 2022, a total of 14 samples were collected (Figure 2).

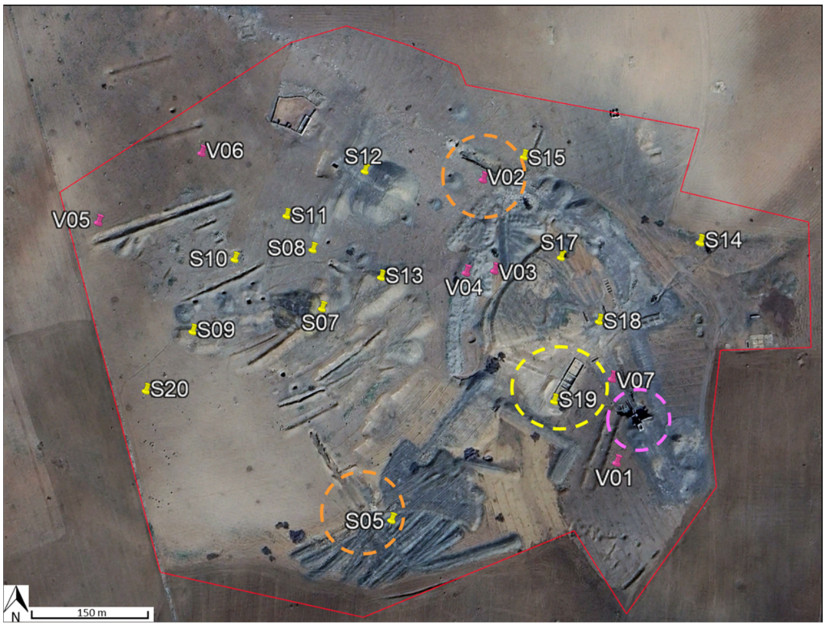

Figure 2. The Sidi Bou Azzouz abandoned mine; locations of the samples collected during the in situ sampling campaigns (in yellow samples collected in May 2022 and in magenta samples collected in June 2023). The orange circles highlight the galleries; the yellow circle depicts setting tanks; and the magenta circle depicts the processing area (Google Earth Pro-Image © Airbus 2025, acquired on 2 February 2022).

Following the collection of GPS coordinates, a total of three to five spatially distributed samples were collected from each stockpile within 10 m.

The sampling strategy was aimed at collecting mining residues from different stockpiles, including, at the same time, the largest heterogeneity occurring in the study area. Stockpiles were first identified matching photointerpretation and knowledge provided by local authorities. During the fieldwork, samples were collected across the whole mining site to consider all unidentified stockpiles. Samples, without any pretreatment, were considered for laboratory reflectance measurements. Samples for subsequent chemical and mineralogical analyses were ground in an agate mortar, passed through a 0.150 mm sieve, and pelletized. Finally, a second sampling campaign was conducted in June 2023, when additional 7 samples were collected with the aim of validating the identification and classification achieved by satellite data, combined with chemical compositional and mineralogical data. The second survey was completed with 18 ground control points, where only field observations were used to validate the photo-interpreted sketch map.

2.3. Hyperspectral Data

Hyperspectral data were used for the identification of CRMs and for assessing the spatial distribution of those deposits. The first task was approached with spectral acquisitions obtained under laboratory conditions on sampled materials. The second task was developed differently, analyzing imagery provided by satellite platforms.

2.3.1. Laboratory VIS-NIR-SWIR Spectroscopy

Spectroscopy is a non-destructive technique used to measure the relative absorption of photons as they interact with minerals across a specific wavelength range, compared to a reference standard [3,36–40]. Hyperspectral signatures are useful for the detailed identification and characterization of materials, exploiting the large amount of data from the visible to short infrared range of the electromagnetic spectrum. In particular, the visible–near-infrared–shortwave infrared (VNIR-SWIR) range yields spectral features that provide valuable insights into the composition and properties of different minerals, as they exhibit characteristic absorption, reflectance, or transmission in these spectral regions.

The spectral signature of each air-dried mining residue sample collected in the abandoned mine, during two different field surveys, has been recorded in the laboratory by reflectance spectroscopy using a field hyperspectral spectrometer (FieldSpec 3, Analytical Spectral Devices—ASD, Boulder, CO, USA) in the VNIR-SWIR spectral domain (350–2500 nm), with a sampling resolution ranging between 1.4 nm in the visible domain and 2 nm in the SWIR domain. In this range, the absorption features are primarily caused by electronic processes occurring between 350 nm and 1300 nm, and vibrational processes occurring above 900 nm [3,36–40]. The measurements were performed using a sensor with a field of view of 25° (bare optic fiber probe) placed approximately 10 cm above the sample, facing vertically downward over the sample, and spanning a surface area of about 15 cm^2. The halogen light source (ASD-Lowel Pro-Lamp) was placed approximately 35 cm from the sample (45° viewing). Fifty acquisitions were acquired and integrated for each measurement. A white Spectralon® panel (a Lambertian reflector) was used as a reference to calculate the reflectance of the sample. The reference panel was therefore measured at the beginning and end of each measurement session, achieving an estimated error of approximately 2% for the absolute reflectance. Finally, shadow effects on each sample were minimized by performing four series of ten measurements, rotating the sample by 90°. Reflectance spectra were then averaged and analyzed using the Savitzky–Golay filter associated with the continuum removal approach, enhancing the detection of spectral absorption features [3]. Furthermore, laboratory spectra were processed to obtain a homogenized dataset coherent with spectral libraries available for minerals and rocks, provided by the United States Geological Survey (USGS) [41] and the Jet Propulsion Laboratory (JPL) [42].

2.3.2. Satellite Hyperspectral Imaging

Data were acquired using two different sensors onboard the PRISMA hyperspectral satellite platform. The VNIR spectrometer yields 66 spectral bands (from 400 nm to 1010 nm) with a nominal spectral sampling interval lower than 11 nm and a bandwidth lower than 15 nm, whereas the SWIR detector acquires 174 spectral bands in the region between 920 and 2500 nm with a bandwidth lower than 15 nm [25].

In this study, a PRISMA L2D image, orthorectified and atmospherically corrected (PRS_L2D_STD) [43] of the abandoned mine area under study was acquired on 28 August 2022 (the overpass closest to the field sampling date). Imagery was downloaded from the PRISMA website (http://prisma-i.it, accessed on 4 May 2025), and the image was processed and analyzed using ENVI 5.6.3 software. Before merging the VNIR and SWIR datasets into a single image file, the overlapping reflectance bands (930–998 nm spectral range) were removed, as well as regions affected by atmospheric interferences [6]. The same identification of spectral features used for laboratory observations was combined with additional statistical analysis aimed at assessing the spatial distribution of the defined spectral endmembers. The dimensionality reduction obtained by the Principal Component Analysis (PCA) was coupled to the Spectral Angle Mapper (SAM) classification, which is a physically based spectral classification that uses an n-D angle to match pixels to reference spectra [27,44]. The algorithm determines the spectral similarity between two spectra by calculating the angle between the spectra and treating them as vectors in a space with dimensionality equal to the number of bands. This technique, when used on calibrated reflectance data, is insensitive to illumination and albedo effects [44]. SAM compares the angle between the endmember spectrum vector and each pixel vector in n-D space. Smaller angles represent closer matches to the reference spectrum. Pixels further away than the specified maximum angle threshold in radians are not classified. The maximum angle threshold applied in the SAM analysis was set to 0.1 radians for each training set [27,44].

The spectral similarity algorithm supported the identification of spectral endmembers, which were considered for the selection of representative region of interest in the available satellite imagery. The obtained spectra were used with a Linear Spectral Unmixing model (LSU), obtaining the relative occurrence of each endmember in the considered pixel. The quality of this result was assessed using the produced error map obtained by using the procedure available in ENVI [45].

2.3.3. Satellite High Spatially Resolved Imagery

Photointerpretation was carried out using the PRISMA panchromatic imagery with a spatial resolution of 5 m per pixel [43], combined with images obtained by Google Earth Pro-Image © Airbus 2025, acquired on 2 February 2022.

2.4. Bulk Mineralogical and Chemical Composition

The identification of mineral phases (iron oxides, calcite, phyllosilicates, silicates), in terms of volumetric percentage, was carried out by XRPD (X-ray Powder Diffractometry) using a Brucker D500 diffractometer with CuKα radiation (n = 1.5418 Å), operating at 40 kV and 40 mA with a step size of 0.0250°. The software used for qualitative analyses was WinPLOTR FullProf Suite (version date October 2006) [46].

The chemical analyses, concerning major elements (SiO_2, Al_2O_3, Fe_2O_3, TiO_2, CaO, MgO, K_2O), were performed using the SPECTRO XEPOS ED-XRF elemental analyzer, optimized for heavy elements with a maximum power of 50W and a voltage of 50 kV. The X-ray EDS fluorescence spectrometer features a Pd/Co alloy anode X-ray tube with air cooling, an adaptive excitation system, and optimized filters. It includes an HAPG (Highly Annealed Pyrolytic Graphite) polarizer for enhanced sensitivity for elements in the Na-Cl range and a bandpass filter for improved performance in the K-Mn range. Signal detection is carried out with an SDD detector cooled by a Peltier system, with a 30 mm^2 detector fiarea and a 20 mm^2 active area. It offers a spectral resolution (FWHM) of 130 eV for Mn Kα and can handle an input count rate of up to 1,000,000 counts per second. Calibration nuilcurves were constructed using international standards and the Lukas-Tooth and Price linear model. Results were compared with those obtained via the TurboQuant method and SPECTRO's calibration model, combining the Fundamental Parameter approach with the Extended Compton scattering model and mass attenuation coefficient calibration. The best calibration curve for each element was selected based on alignment with the given concentrations of international standards.

The estimation of the Loss on Ignition (LOI) was performed at 1000 °C with the final aim of assessing the organic carbon content [47].

2.5. Petrographic Features and Mineral Composition

The microscopic distribution of elements and, consequently, the identification of mineralogic patterns were obtained by SEM back-scattered-electron (BSE) images, energy dispersive X-ray (EDS) spectra, and X-ray maps. Data were acquired on selected portions of samples coated with a conductive layer (about 200 Å thick) of graphite using a ZEISS EVO MA10 SEM. This SEM was equipped with an Oxford X-Max detector for EDS analysis, operating at a 20 kV acceleration voltage and using a LaB6 crystal source, which enabled high-quality imaging and semi-quantitative elemental analysis [48].

2.6. Laser-Induced Breakdown Spectroscopy

Laser-Induced Breakdown Spectroscopy (LIBS) is a type of atomic emission spectroscopy, which is a chemical analysis method that measures the light emitted by plasma. The lightest elements, such as H, He, Li, Be, B, C, N, O, Na, and Mg, which can be present in geomaterials at high concentrations but are challenging to measure using other analytical techniques (e.g., XRF), are exceptionally sensitive to LIBS [49]. About 20 years ago, handheld (hLIBS) instruments were introduced, creating the opportunity to perform on-site geochemical analysis in the field.

The SciAps Z-903 (Woburn, MA, USA) hLIBS instrument used in this study was described in detail by previous research [50]. Briefly, the instrument includes a proprietary Nd-YAG diode-pumped solid-state pulsed nanosecond laser operating at a wavelength of 1064 nm that delivers a 5–6 mJ laser pulse of 1 ns duration with a nominal 100 µm beam size at a 10 Hz firing rate. The plasma light was collected and transferred by fiber optic cables to three spectrometers equipped with time-gated, charge-coupled detectors (CCDs), which record the spectra in a wavelength acquisition range from 190 to 950 nm, covering the ultraviolet (UV) to visible and near-infrared (VNIR) range.

All hLIBS analyses were performed in ambient air under a constant Ar purge, with a delay time fixed at 650 ns at the beginning of the acquisition of the LIBS emission and an acquisition time window fixed at 3 ms. The qualitative composition analysis of the samples was performed by firing one prior laser cleaning shot and then four measuring laser shots on twelve points located in three randomly selected rectangular areas where the LIBS grid pattern was positioned on the sample surface. In this way, a total of 144 LIBS spectra were measured, and 36 average LIBS spectra were recorded for each sample.

3. Results

3.1. Laboratory Spectroscopy

The main target of hyperspectral observations under laboratory conditions was the identification of spectral features in different samples associated with the occurrence of CRMs. The first task was aimed at isolating the major components explaining the variance observed in the dataset associated with the first field survey. Laboratory conditions are ideal for avoiding atmospheric interferences during the measurements, to enhance the signal-to-noise ratio produced by the instrument and, finally, to provide a higher spectral resolution compared to spaceborne sensors. Key spectral features were identified as major discrimination metrics between different surface types (Figure 3a).

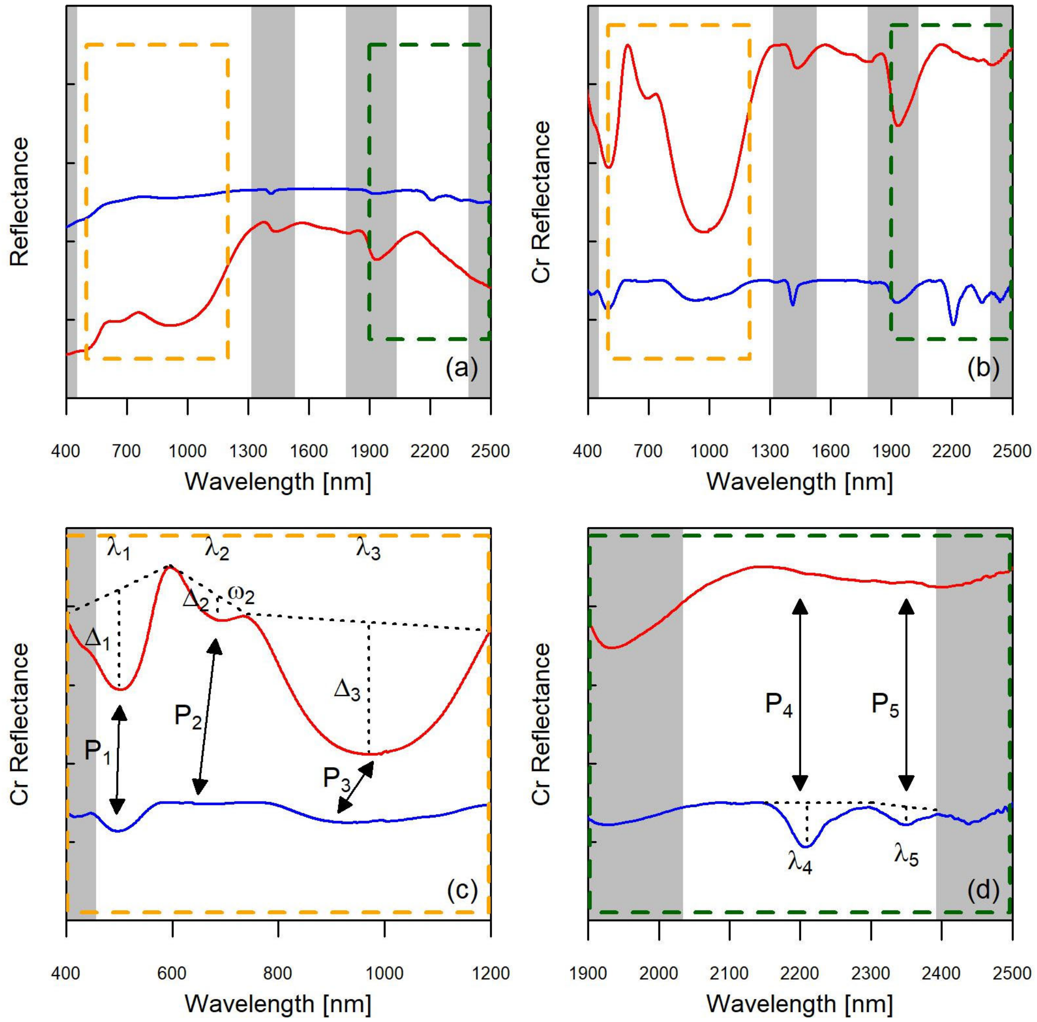

Figure 3. Stacked reflectance (**a**) and continuum-removed (Cr) spectra (**b**) of selected deposit sampled area (S15 in red and S7 in blue). Representation of the spectral features considered in the VNIR domain (**c**) and in the SWIR region (**d**). Gray spectral regions represent the ranges where atmospheric interferences occur on satellite data.

These features were described by processing the continuum-removed spectra (Figure 3b) in terms of their maximum absorption wavelength (λ_i), by the absorption peak depth (Δ_i), and by the baseline slope (ϖ_i). Some of them were defined in the extended visible–near-infrared domain (VNIR), where iron-bearing minerals significantly affect the spectral behavior of different samples. Several spectral features in the VNIR range are, in fact, associated with charge transitions related to the ferric iron, which impact the relative intensity of each absorption peak (Figure 3c). The occurrence of iron-related features was detected at ~500, ~670, and ~970 nm in agreement with the documented literature. The first three peaks (P_1, P_2, and P_3) showed two distinct patterns with deep (higher than 20%, 1%, and 10%, respectively) or shallow depths (Table 1).

Table 1. Summary of the average metrics derived for each surface type.

Spectral Features		**A1**	**A2**	**B1**	**B2**	**B3**
P_1	λ_1 [nm]	508	508	497	494	495
	Δ_1 [%]	25.5	22.4	10.1	11.4	3.3
P_2	λ_2 [nm]	686	698	661	664	643
	Δ_2 [%]	7.8	3.3	1.0	0.6	0.5
	ϖ_2 [%]	−2	−9.7	0	0	0
P_3	λ_3 [nm]	964	1010	939	960	923
	Δ_3 [%]	41.3	46.4	8.4	7.3	4.0
P_4	λ_4 [nm]	2207	2210	2204	2207	2207
	Δ_4 [%]	1.6	0.5	9.2	9.8	8.5
P_5	λ_5 [nm]	2379	2347	2392	2348	2342
	Δ_5 [%]	1.6	4.2	3.9	3.3	2.2

In contrast, those samples characterized by shallower VNIR peaks showed a deep behavior on P_4 with a depth higher than 10%. The P_4 absorption peak located at ~2200 supported in this case the detection of Al-bearing mineral phases [16,17]. Combining all this evidence, it was possible to distinguish between iron-dominated samples (A) and Al-occurring deposits (B).

Additional separations were possible, looking at the relative configuration of VNIR peaks P_2 and P_3 in group A. Those Al-free samples are influenced by the distribution of iron-related absorptions between 600 and 800 nm. Two different behaviors were detected, and the baseline slope of P_2 introduced an additional separation level between flat (A1) and sloped (A2) behaviors ($\varpi_2 < -5\%$), as summarized in Table 1. Similarly, group B showed an additional spectral feature based on the absorption peak at about 2300 nm (P_5). The spectral behavior in the SWIR domain is influenced by primary and secondary Al-OH features, as well as by additional overtones associated with CO_3. The increasing content of carbonate minerals impacts on λ_5, which shifted by about 50 nm from B2 to B1 subgroups. The picture was completed by an outlying behavior of a single sample composed of aluminosilicates, where a particular spectral feature was detected after P_3. That peak was coupled to an additional absorption feature located at about 1000 nm, suggesting the definition of a third B subgroup (B3) [16,17].

The identification of the proposed spectral end members highlighted the opportunity to search in satellite data for the same categories (Figure 4), evaluating the possibility of identifying the same features using observations affected by atmospheric interferences and sensor signal-to-noise issues.

3.2. Satellite Analysis

The identification of spectral end members from laboratory spectroscopy supported the analysis of satellite data obtained by PRISMA. Spaceborne spectra of the sampling sites showed a similar behavior in the VNIR range, characterized by increasing reflectance values (Figure 5).

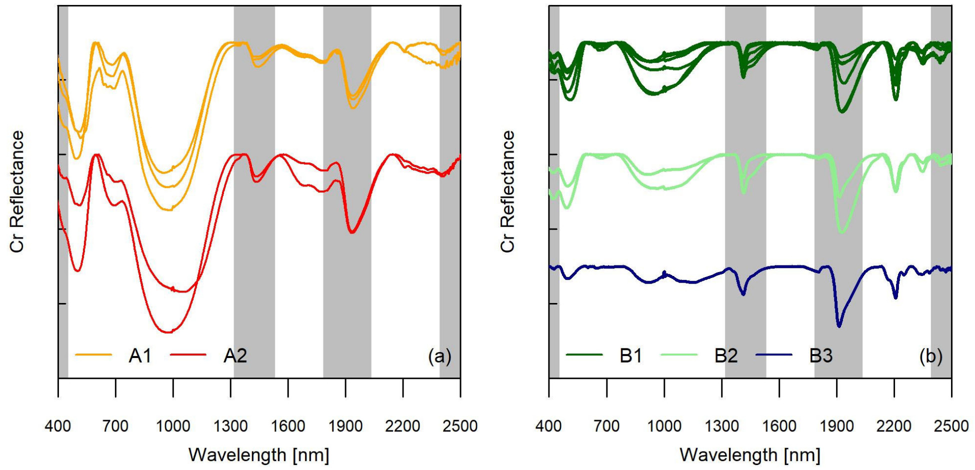

Figure 4. The hyperspectral signatures obtained under laboratory conditions for groups A1 and A2 (**a**), separated by groups B1, B2, and B3 (**b**).

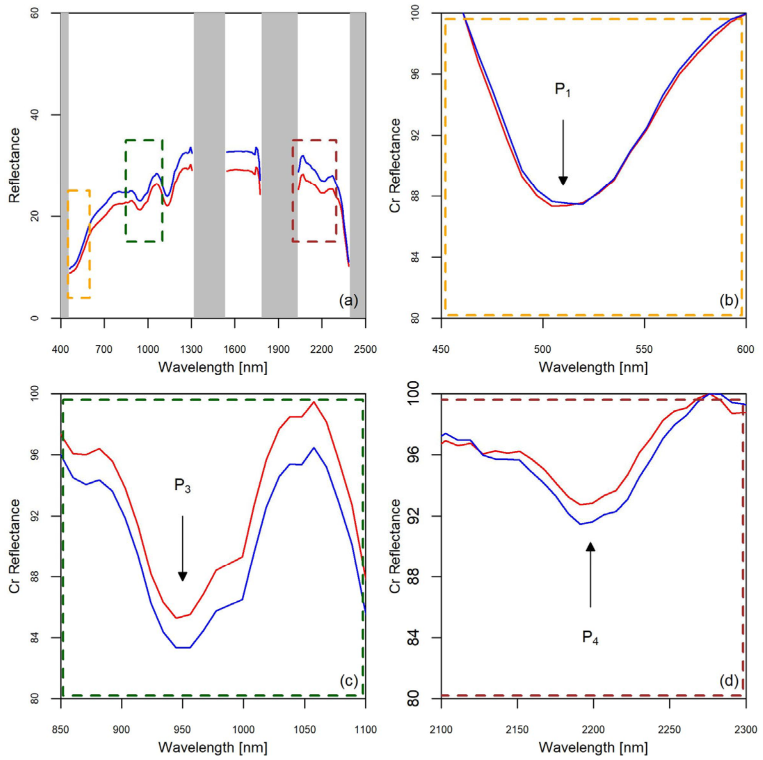

Figure 5. Examples of PRISMA hyperspectral signatures in the sampling site (**a**), associated with specific spectral features (**b**–**d**) highlighted by dotted lines in all panels. Selected samples are S5 (blue) and S17 (red).

The spectral features defined in Section 3.1 were recognized even in satellite data and supported the discrimination between groups A and B, only in terms of iron oxides and aluminosilicate occurrences. Such observations are consistent with other studies, where those features were selected for assessing the distribution of quartzite and carbonates [6]. PRISMA data are unfortunately affected, as most of the hyperspectral sensors are, by instrument noise [51], which limits the detection of narrow spectral features on stockpiles composed of heterogeneous reworked materials. From this perspective, enhancing the discrimination of mineralogical composition using satellite data required the removal of the sensor noise contribution [52] and the reduction in spectral dimensionality through optimized spectral components. This goal was approached using the Principal Component Analysis (PCA), which is a basic tool focused on identifying the major features observable from multidimensional datasets. The eigenvalues observed for the first 13 principal components (PCs) showed that the first three components account for more than 88% of the variance (Table 2). The first component accounts for the largest fraction of variability, associated with higher loading factors located from the NIR domain to the SWIR region (Figure S1). This result confirms the multicollinearity and redundancy of spectral measurements, where the overall albedo is controlled by the granulometric composition and the dominant mineralogical composition. Nevertheless, the second and third components are related to more specific spectral features, with the second being controlled by wavelengths in the visible region and the third by wavelengths positioned at 1300 nm and 1600 nm (Figure S1).

Table 2. Results of PC1, PC2, and PC3 applied to PRISMA image.

PC	Eigenvalue %	Variance %
1	94.82	82.50
2	3.3	5.37
3	0.57	0.65

The score values of the sampling sites served as a training set for the SAM classification, enabling the spatial assessment of distinct classes or typologies of areas containing mining residues potentially of interest. The SAM supported the identification of spectral endmembers, which were used to perform LSU (Figure 6).

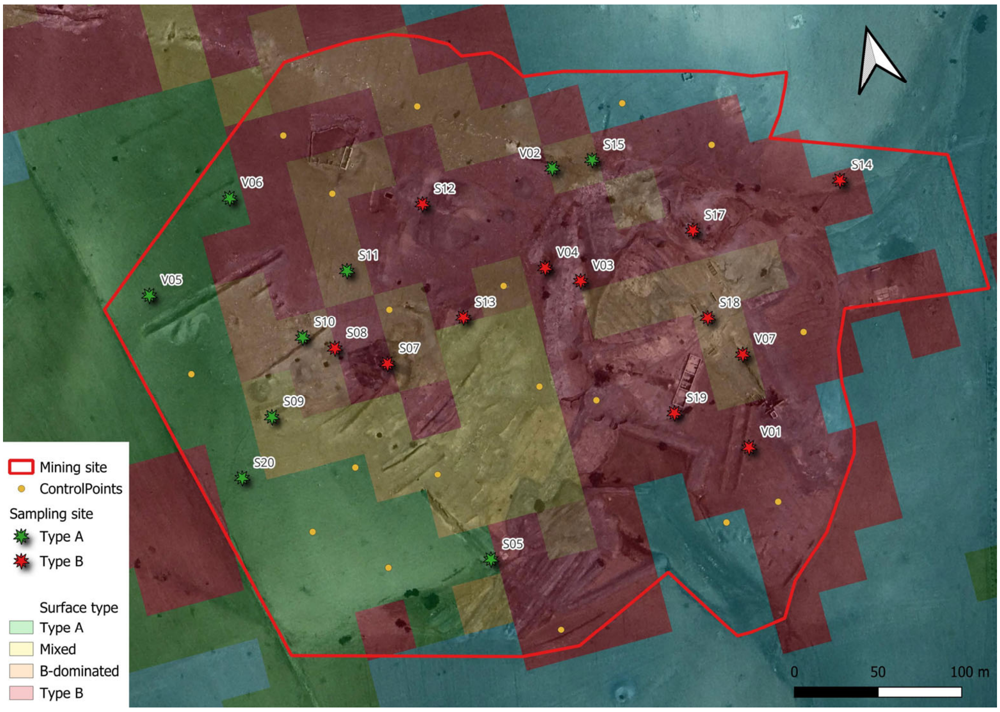

Figure 6. Spatial distribution of the mining residue classes. Identified classes are overlaid on a high-resolution image obtained by using Google Earth Pro-Image © Airbus 2025, acquired on 2 February 2022.

The obtained classification produced a map of mining waste deposits, tailings, and undisturbed soils, where pixels were associated with the different end members or mixtures of them. LSU provided pixels with the occurrence of single-end members with more than 60% of type A, type B, or undisturbed soils. Finally, the discrimination between A1 and A2, or between B1, B2, and B3, based on spectral features, was not possible since the SWIR range above 2200 nm was strongly affected by sensor noise. Considering the interest towards group B, intermediate levels of occurrence were identified with B-dominated areas (type B between 30% and 60%) and uncertain mixed areas (without a dominant component).

3.3. Bulk Chemistry and Mineralogy

The interpretation of the spectral end members previously identified was produced using chemical and mineralogical analyses on sampling sites grouped from the spectral point of view (Table 3). The chemical composition of the different clusters showed significant differences in terms of silica content as well as iron oxides. Although group A1 was silica-dominated ($SiO_2 > 80\%$), clusters B1, B2, and B3 were characterized by lower amounts of silica. The lowest amount of SiO_2 was detected in group A2, which highlighted the highest amount of iron oxides (>50%). Significant levels of Al_2O_3 were detected only in clusters B1, B2, and B3, which were also associated with different amounts of alkaline elements (Li, Na, Rb, and K). The occurrence of Ca in groups A2 and B2 is notable, as it is strongly related to the presence of carbonates and/or scheelite (a calcium tungstate mineral), indicated by the Loss on Ignition (LOI).

Table 3. Average content of major elements in different clusters.

Content [wt%]	A1	A2	B1	B2	B3
SiO_2	83.93	36.00	65.14	54.80	57.01
Al_2O_3	0.84	1.21	15.54	15.77	19.97
Fe_2O_3	12.72	51.20	7.11	10.44	6.51
TiO_2	0.03	0.02	0.59	0.65	0.92
CaO	0.15	2.73	1.31	4.24	2.43
MgO	0.14	0.30	1.59	2.25	2.95
K_2O	0.15	0.14	5.01	3.93	4.39
L.O.I.	1.80	7.99	3.17	7.28	4.42

From this perspective, the mineralogical composition confirmed the presence of Fe^{3+}, and Al-OH elements were associated with the occurrence of goethite and muscovite minerals (Table 4). In the hydrothermal deposits of alkaline granitic rocks, these elements can also be associated with ore deposits of wolframite $(Fe,Mn)WO_4$, an iron, manganese, and tungstate mineral. From a general point of view, chemical and mineralogical analyses did not evidence mineral phases with significant levels of historically exploited elements (W, Cu). Samples belonging to group A1 are composed exclusively of quartz, with concentrations even higher than 90%. However, the XRPD analysis revealed the presence of goethite, confirmed by significant Fe_2O_3 content. The occurrence of muscovite was also detected by XRPD, although this phase is present in low amounts, as indicated by the low concentration of alumina and K_2O, which are, respectively, lower than 1 wt% and 0.5 wt%.

The semiquantitative amounts of white mica with Li (Li-bearing white mica) in B1 cluster samples revealed by XRPD range from about 20% (sample S13) to about 60% (sample S08). It highlights that goethite mostly occurs in sample S17, characterized by an Fe_2O_3 concentration of about 12%, which is about double the concentration present in the other samples. The presence of a significant amount of limonite in the two samples of the A2 group is confirmed, with a minor occurrence of calcite. Group B2 differed from other samples by the presence of white mica with Li, calcite, and chlorite as the main diagnostic minerals. Class B3 is the sole sample where muscovite and goethite are negligible, and biotite is the major phase, associated with chlorite. It is important to note the significant amount of oligoclase in this sample.

Table 4. Average mineralogical composition obtained by XRPD.

Content [vol%]	A1	A2	B1	B2	B3
Goethite	2.11	-	5.80	4.94	-
Limonite	-	12.42	-	-	-
Muscovite	4.44	-	-	-	-
Biotite	-	-	-	-	26.27
Chlorite	-	-	-	3.62	5.06
Calcite	-	5.99	-	2.28	-
Li-bearing white mica	-	-	41.54	37.93	-
Quartz	93.45	84.59	51.16	51.23	56.88
Plagioclase	-	-	6.06	-	11.79

3.4. Microscopic Chemistry

SEM-EDS results confirmed the mineralogical composition obtained by the other investigations. For instance, the SEM-EDS analysis results of group B1 also evidenced the presence of a "titanate", i.e., an oxide of Ti, Fe, and Mn (Figure 7), because titanium metal is included in the Critical Raw Materials Act 2023 of the European Union [7].

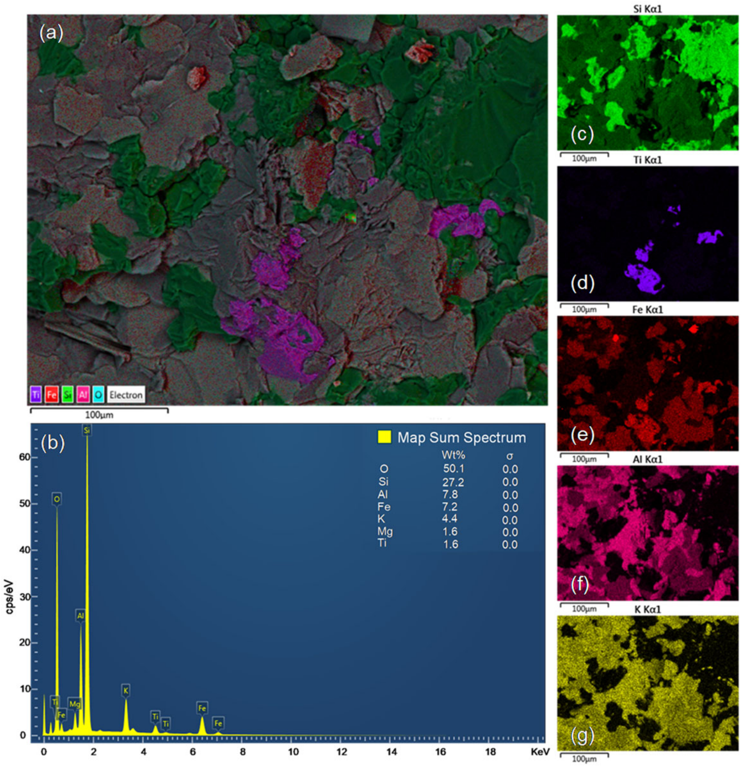

Figure 7. Example of SEM-EDS results for a class B1 sample. Combined elemental maps (**a**) and an abundance plot (**b**) are associated with single element patterns (**c**–**g**).

This could be of economic and strategic importance for industry and the green transition. However, this phase occurs in low amounts, as testified by the titanium (TiO_2) concentration (about 1.6 wt%) in the samples of cluster B1, values too low to be observed in the spectral signatures. SEM-EDS results, particularly X-ray compositional maps, confirm the presence of goethite in all B1 samples.

It is worth highlighting that all LIBS spectra detected the characteristic emission peak of Li at 670.8 nm (Figure 8). Samples with this Li-related peak were all those constituting group B1 and B2. Lithium might be present in the white mica, probably the lepidolite mineral.

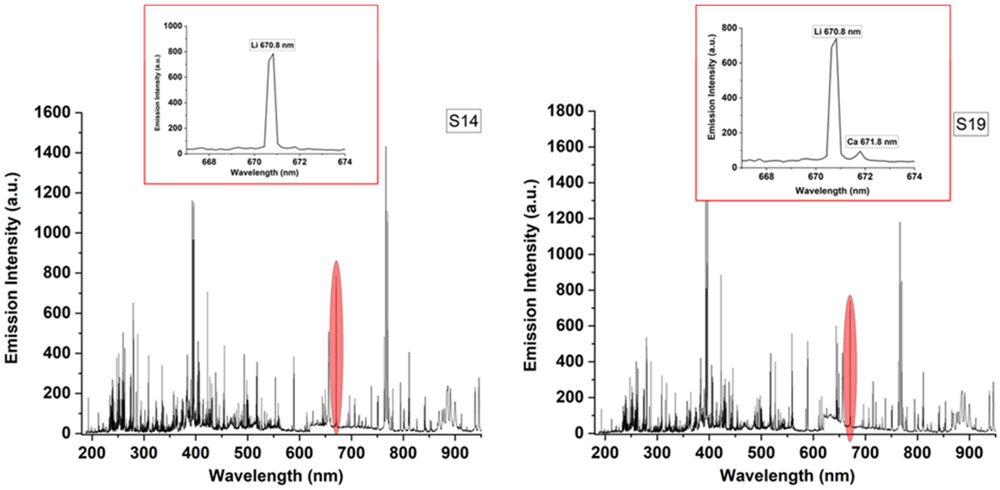

Figure 8. Examples of LIBS results for group B1 and B2, where the Li occurrence is confirmed.

4. Discussion

The interpretation of produced results supported the answer to two major questions: which mining residues are potentially reusable? What is the spatial distribution of those deposits?

4.1. Characterization of Residues

The first question was approached considering the spectral behavior of minerals (Figure 9) provided by the USGS spectral library under laboratory conditions. Such spectral signatures supported the interpretation of data obtained on sampled materials characterized in the laboratory using the Fieldspec instrument.

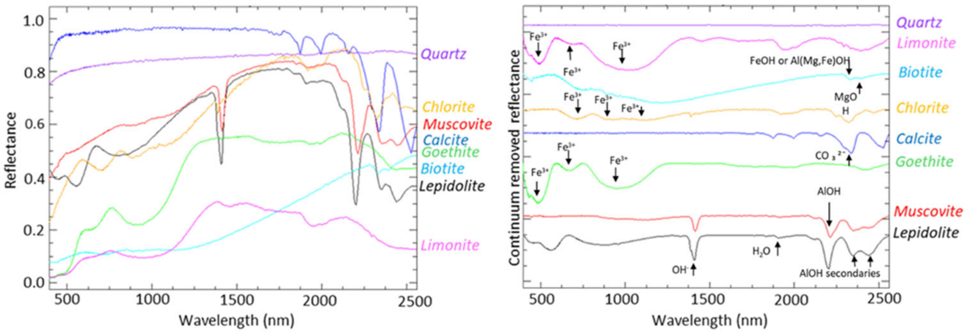

Figure 9. The main minerals are from the USGS spectral library. On the left are the reflectance curves, and, on the right, there are the continuum-removed curves with the main absorption peaks.

While spectral features in the VNIR domain, with reference to Fe^{3+}-related peaks, supported the identification of goethite-like minerals, Al-OH absorption peaks highlighted the occurrence of white mica. All these features evidence the potential occurrence of lepidolite, which is confirmed only by the detection of Li in the mineral structure. From the hyperspectral point of view, field, and remote sensing observations, even if associated with high values of quartz (from ~51% to ~93%) in the samples, presented spectral behaviors where diagnostic minerals were clearly evidenced by their main absorption features.

Starting from the average spectrum of class A1, obtained under laboratory conditions and presented in Table 1, continuum-removal highlighted the distinctive VNIR features at ~485 nm, ~670 nm, and ~950 nm associated with ferric iron (Fe^{3+}). While the NIR domain was characterized by a wide spectral width of a 950 nm Fe^{3+}-related peak, typical of iron hydroxide phases, the SWIR region was affected by a limited contribution of Al-OH peaks. Such a peculiar pattern suggested the contribution of two minerals, such as goethite and muscovite [3,53,54], with different proportions. XRPD confirmed a quartz-dominated framework where LIBS neglected the occurrence of Li minerals.

Reflectance and continuum-removed spectra of the A2 class evidenced weak absorption in the SWIR region but marked spectral features associated with the presence of limonite (Table 1). Limonite was originally considered as a species but now is described as an iron oxyhydroxide with a poor crystalline character, and it consists of cryptocrystalline goethite [16,17]. The absorption peaks of limonite are evidenced by its specific VNIR features (~490 nm, ~690 nm, and ~980 nm due to ferric iron absorptions).

From a general point of view, traditional analyses were more efficient in detecting the occurrence of tiny amounts of calcite (<10 wt%), compared to results obtained by hyperspectral measurements. This behavior was associated with differences in sample pretreatment, where calcite was present in the finest size component of samples, contributing less to the spectral behavior of samples.

The spectra of class B1 showed (Table 1) in the SWIR region the typical white mica features in the continuum-removed curves. In particular, the main absorptions have been identified in the spectrum: peak around ~1409 nm due to OH^- (hydroxide ion) associated with the main sharp Al-OH peak (between 2195 nm and 2205 nm) and the shallow Al-OH secondary features at ~2348 nm and ~2435 nm [3,16,17,53,54]. The VNIR region was characterized by multiple absorption peaks at ~430, ~485, ~670 nm, and ~950 nm, together with the drop off to extreme blue in the reflectance curves, which are related to ferric iron and manganese [3] overtones. Such features were interpreted with the occurrence of goethite and a negligible presence of white mica. Spectral measurements highlighted a significant probability of having Li-bearing minerals, and results obtained by LIBS analysis confirmed the Li-rich behavior of such deposits. However, the discrimination between lepidolite from Li-bearing white mica is out of the scope of this work, and further in-depth chemical and mineralogical analyses will be carried out to support the identification of additional opportunities for characterizing these mineral phases in selected samples.

Regarding the average spectra of class B2 (Table 1), the VNIR absorptions related to ferric iron (Fe^{3+}) at ~430, ~485, ~670 nm, and ~950 nm evidence the presence of goethite. In the SWIR region, even the diagnostic features of white mica characterized the continuum-removed curve of class B2 with a peak around ~1409 nm due to OH^- (hydroxide ion) associated with the main sharp Al-OH peak between 2195 nm and 2205 nm and the shallow Al-OH secondaries features at ~2348 nm and ~2435 nm [3,53]. The occurrence of Li was also confirmed in this case by LIBS.

Finally, the sample of type B3 showed a slightly different spectral behavior, where a shallower and broader peak in the NIR region can be associated with biotite (Table 1) [3,16,17,53,54]. Secondary and less inflected peaks can be potentially observed, but further investigations must be conducted to detect additional phases identified with traditional mineralogical techniques (chlorite).

The occurrence of the main mineralogical phases marked by absorption spectral features is reported in Table 5, and it summarizes the mineralogical composition of five groups.

Table 5. Synthesis of the main mineralogical composition of 5 groups highlighted by ASD. Detected mineral phases are marked with X.

ASD	A1	A2	B1	B2	B3
Goethite	X		X	X	
Limonite		X			
Biotite					X
Chlorite				X	
Li-bearing white mica			X	X	
Muscovite	X				X

The mining residues of class B1 and B2 are characterized by the presence of the white mica with Li, and they are the most interesting deposits considering that lithium is involved in the Critical Raw Materials Act, 2023 [7].

4.2. Spatial Distribution of Residues with Li-Bearing White Mica

Matching geochemistry, mineralogy, and hyperspectral measurements, it was possible to identify a zone associated with A1 samples where mining residues were coarse materials containing goethite and muscovite. Class A2 included pixels located near galleries, and deposits were strongly dominated by limonite. The class related to B1 samples included stockpiles accumulated in open areas, where goethite and Li-bearing white mica were significantly present. Mining residues identified as class B2 represented the oldest stockpiles associated with mining activities that ceased approximately 40 years ago; they were characterized by the occurrence of goethite, white mica with Li, and chlorite. Finally, class B3, which was identified as a separate category with a unique mineralogical composition, was dominated by biotite and accessory mineral phases. Coupling such a description to the LIBS evidence, it was possible to highlight the potential occurrence of deposits of interest by a significant amount of Li. Furthermore, classes B1 and B2 exhibited the highest content of white mica with Li and cover the largest areas (47% with more than 60% of type B materials and 16% of dominated deposits with more than 30% of those residues). In contrast, classes A1 and A2 occupy smaller areas (less than 26% of the total mining area) but are distinctly separate from each other. These smaller classes represented the oldest mining residual deposits in the mine. The presence of limonite in class A2 suggested that these stockpiles have been exposed for a longer time compared to the more extensive B1 and B2 classes. Notably, 11% of the surface in the mining site showed a significant uncertainty in the identification of a clear dominant component.

The validation of the obtained classification was carried out using data provided by a second field campaign conducted in 2023, where field observations were combined with high spatially resolved imagery. Considering nine samples and six control points of tailings with an interesting content of CRMs, it was possible to identify stockpiles exclusively constituted by Al-bearing materials correctly. Such areas represented locations where mining activities processed exploited materials by grinding and crushing. Stockpiles were characterized by finer size distributions, from 90% of gravel near preprocessing facilities to less than 10% around the separation basins. Although six points were correctly associated with materials dominated by type B residues, five quartz-dominated samples were collected close to exploited areas, within 5 m of the observed features (galleries or trenches). Pixels in this case were classified as Type B-dominated deposits with mixed materials, with Al-bearing materials occurring between 30% and 60%. Those areas were characterized by larger fractions of surfaces with gravel deposits (where type B materials were detected), with patches of debris adjacent to excavations. This behavior represented a limitation for the use of 30m resolution hyperspectral data, but additional in situ or airborne hyperspectral surveys will surely fill such a gap. While the identification of a dominant composition was possible, a significant fraction of the mining site, about 11% of the area, was affected by uncertain mixing issues that satellite data were not able to solve. Two control points and one type A deposit were observed in the uncertain mixed area where stockpiles were topographically elevated, and spectral observations made from spaceborne platforms were strongly affected by surface roughness. Finally, less interesting deposits and undisturbed soils were detected in the peripheral zones of the mining site, with 10 control points where materials were poor in terms of potential CRMs.

Considering the image classification, the geological survey carried out during the second field campaign allowed the creation of a sketch map of the mining residues accumulation zones for the identification of white mica with Li contents (Figure 10). Zones with accumulated B1 and B2 deposits are therefore the areas with mining residues whose content can be considered of interest such as raw materials.

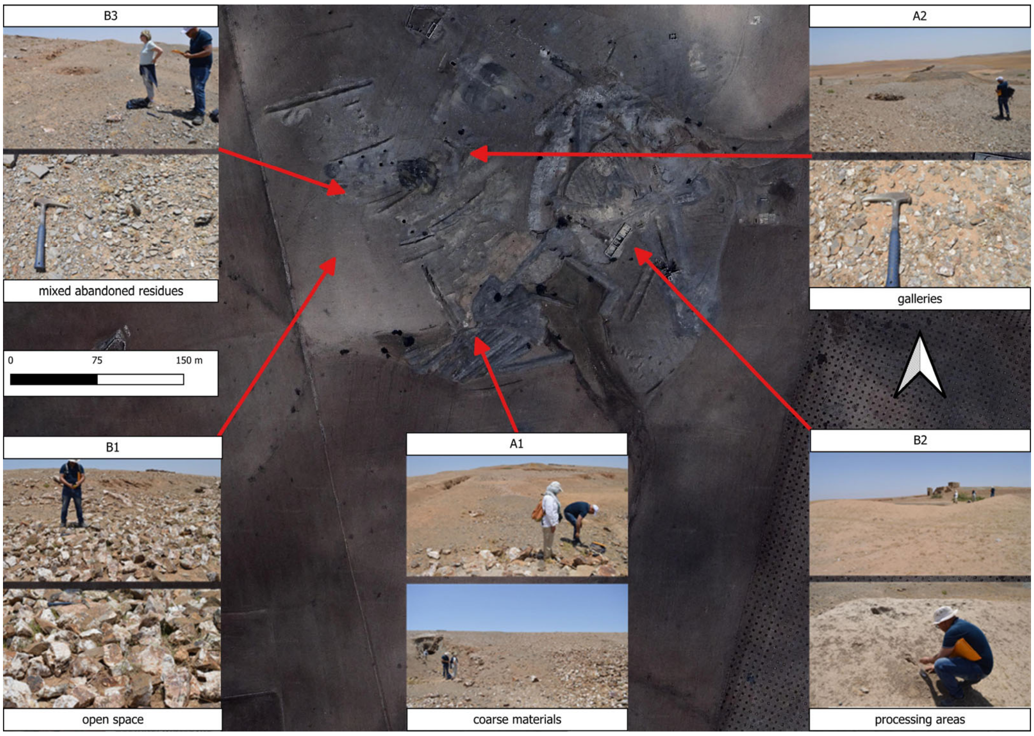

Figure 10. The spatial distribution of mining residues identifying different zones (red arrows) with varying mineralogical compositions in the Sidi Bou Azzouz abandoned mine (Google Earth Pro-Image © Airbus 2025, acquired on 2 February 2022).

5. Summary and Conclusions

The Sidi Bou Azzouz abandoned mine still holds significant potential as a resource for raw materials. This area, like other mining areas of the southern Rehamna massif of the western Meseta region of Morocco, hosts hydrothermal deposits in lithological outcrops devoid of vegetation and is therefore well exposed, making it a privileged site for the application of an integrated approach of petrographic and geochemical investigations with advanced hyperspectral exploration techniques using satellite imagery and therefore ideal for testing the ability of PRISMA spectral data to identify mining areas in a strategic region for the supply of CRM. Therefore, this research presents an interdisciplinary approach aimed at exploring the capability of PRISMA hyperspectral satellite imagery to identify, classify, and map mining residues with different chemical composition and mineralogical content.

Hyperspectral data highlighted the occurrence of stockpiles where exploitable CRMs are present; for instance, Li-bearing white mica is a potential source of interest. These spectral data agreed with chemical and mineralogical results, which confirmed that the PRISMA satellite data were appropriate to assess the spatial distribution of different minerals present in the mining residues of the study area. This result underscored the potential of hyperspectral remote sensing as a tool for mineral exploration and environmental monitoring, especially in areas where ground-based sampling may be difficult or impractical. The proposed approach considered two different layers of spectral observations, which included two completely different spatial scales (satellite-based and laboratory). Additional intermediate observations, provided by different satellite or airborne sensors, will fill the gap between coarse and in situ measurements.

This interdisciplinary approach offers a promising method for resource exploration and environmental assessment, with applications that can extend to both the mining industry and environmental monitoring. Spatial resolution was surely a limiting factor, but additional in situ hyperspectral surveys (ground-based or airborne) will surely complete the proposed preliminary picture.

Supplementary Materials: The following supporting information can be downloaded at https://www.mdpi.com/article/10.3390/rs17111838/s1, Figure S1: Loading factors for each principal component in relation to the different wavelengths.

Author Contributions: Conceptualization, D.G., R.S. (Roberto Salzano) and R.S. (Rosamaria Salvatori); methodology, D.G. and R.S. (Roberto Salzano); validation, D.G., R.S. (Roberto Salzano), G.S.S., A.W., C.V., A.M.C., M.P., R.P. and R.S. (Rosamaria Salvatori); formal analysis, D.G., R.S. (Roberto Salzano), G.S.S., A.W., C.V., A.M.C., M.P., R.P. and R.S. (Rosamaria Salvatori); investigation, D.G., A.W. and A.M.C.; resources, D.G., R.S. (Roberto Salzano), G.S.S., A.W., C.V., A.M.C., M.P. and R.S. (Rosamaria Salvatori); data curation, D.G., R.S. (Roberto Salzano), G.S.S., A.W., C.V., A.M.C., M.P. and R.S. (Rosamaria Salvatori); writing—original draft preparation, D.G., R.S. and R.S. (Rosamaria Salvatori); writing—review and editing, D.G., R.S. (Roberto Salzano), G.S.S., A.W., C.V., A.M.C., M.P., R.P. and R.S. (Rosamaria Salvatori). All authors have read and agreed to the published version of the manuscript.

Funding: This research was funded jointly by the Consiglio Nazionale delle Ricerche (CNR) of Italy and by the Centre National pour la Recherche Scientifique et Tecnique (CNRST) of Morocco, with the funding reference 0087419-2021.

Data Availability Statement: The data presented in this study are available upon request from the corresponding author due to research objectives.

Acknowledgments: We would like to thank Stefano Stellino for having carried out XRPD analyses at Sapienza Università di Roma. Furthermore, the authors are grateful for the support with chemical and mineralogical analyses provided by the joint laboratory of CNR-IGAG and Sapienza (hosted in the Earth Sciences Department) of Microanalysis and electron Microscopy (LaM2), the laboratory of chemical analysis of CNR-IGAG, and the laboratory of applied petrography of Università degli Studi di Ferrara. Hyperspectral satellite data were processed by the authors under a license from ASI Original PRISMA Product—© Italian Space Agency (ASI)—(2022).

Conflicts of Interest: The authors declare no conflicts of interest.

References

1. Kasmaeeyazdi, S.; Dinelli, E.; Braga, R. Mapping Co–Cr–Cu and Fe Occurrence in a Legacy Mining Waste Using Geochemistry and Satellite Imagery Analyses. *Appl. Sci.* **2022**, *12*, 1928–1939. [CrossRef]
2. Ewais, M.M.M.; El Zalaky, M.A.; Selim, A.Q.; Abu Sharib, A.S.A.A. Implementation of ASTER data for lithologic and alteration zones mapping: Derhib area, South Eastern Desert, Egypt. *J. Afr. Earth Sci.* **2022**, *196*, 104725–104738. [CrossRef]

3. Cardoso-Fernandes, J.; Silva, J.; Perrotta, M.M.; Lima, A.; Teodoro, A.C.; Ribeiro, M.A.; Dias, F.; Barrès, O.; Cauzid, J.; Roda-Robles, E. Interpretation of the Reflectance Spectra of Lithium (Li) Minerals and Pegmatites: A Case Study for Mineralogical and Lithological Identification in the Fregeneda Almendra Area. *Remote Sens.* **2021**, *13*, 3688–3722. [CrossRef]
4. Peyghambari, S.; Zhang, Y. Hyperspectral remote sensing in lithological mapping, mineral exploration, and environmental geology: An updated review. *J. Appl. Remote Sens.* **2021**, *15*, 031501–031526. [CrossRef]
5. van der Werff, H.; van der Meer, F. Sentinel-2A MSI and Landsat 8 OLI Provide Data Continuity for Geological Remote Sensing. *Remote Sens.* **2016**, *8*, 883–899. [CrossRef]
6. Chirico, R.; Mondillo, N.; Laukamp, C.; Mormone, A.; Di Martire, D.; Novellino, A.; Balassone, G. Mapping hydrothermal and supergene alteration zones associated with carbonate-hosted Zn-Pb deposits by using PRISMA satellite imagery supported by field-based hyperspectral data, mineralogical and geochemical analysis. *Ore Geol. Rev.* **2023**, *152*, 105244–105268. [CrossRef]
7. European Commission: Directorate-General for Internal Market, Industry, Entrepreneurship and SMEs; Grohol, M.; Veeh, C. *Study on the Critical Raw Materials for the EU 2023—Final Report*; Publications Office of the EU: Luxembourg, 2023. Available online: https://op.europa.eu/en/publication-detail/-/publication/57318397-fdd4-11ed-a05c-01aa75ed71a1/language-en (accessed on 21 May 2025).
8. Vidal, O.; Weihed, P.; Hagelüken, C.; Bol, D.; Christmann, P.; Arndt, N. *ERA-MIN Research Agenda*; 2013; pp. 1–125. Available online: https://insu.hal.science/insu-00917653v1 (accessed on 21 May 2025).
9. Fetting, C. The European Green Deal. *European Sustainable Development Network (ESDN Report)*; 2020. Available online: https://www.esdn.eu/fileadmin/ESDN_Reports/ESDN_Report_2_2020.pdf (accessed on 21 May 2025).
10. García-Gusano, D.; Iribarren, D.; Munoz, I.; Arrizabalaga, E. The future need for critical raw materials associated with long-term energy and climate strategies: The illustrative case study of power generation in Spain. *Energy* **2025**, *314*, 134266. [CrossRef]
11. Baldassarre, B.; Buesa, A.; Albizzati, P.F.; Jakimow, M.; Saveyn, H.; Carrara, S. *Analysis of Circular Economy Research and Innovation (R&I) Intensity for Critical Products in the Supply Chains of Strategic Technologies*; Publications Office of the European Union: Luxembourg, 2023. [CrossRef]
12. International Energy Agency (IEA). *Global Critical Minerals Outlook 2024*; IEA Publications: Paris, France, 2024. Available online: https://www.iea.org/reports/global-critical-minerals-outlook-2024 (accessed on 21 May 2025).
13. Baldassarre, G.; Fiorucci, A.; Marini, P. Recovery of Critical Raw Materials from Abandoned Mine Wastes: Some Potential Case Studies in Northwest Italy. *Mater. Proc.* **2023**, *15*, 77. [CrossRef]
14. Silva, M.; Hermosilla, G.; Villavicencio, G.; Breul, P. Automated Detection and Analysis of Massive Mining Waste Deposits Using Sentinel-2 Satellite Imagery and Artificial Intelligence. *Remote Sens.* **2023**, *15*, 4949. [CrossRef]
15. European Commission. *Communication from the Commission to the European Parliament, the European Council, the Council, the European Economic and Social Committee and the Committee of the Regions*; A Secure and Sustainable Supply of Critical Raw Materials in Support of the Twin Transition; European Commission: Brussels, Belgium, 2023.
16. van der Meer, F.D.; van der Werff, H.M.A.; van Ruitenbeek, F.J.A.; Hecker, C.A.; Bakker, W.H.; Noomen, M.F.; van der Meijde, M.; Carranza, E.J.M.; de Smeth, J.B.; Woldai, T. Multi- and hyperspectral geologic remote sensing: A review. *Int. J. Appl. Earth Obs. Geoinf.* **2012**, *14*, 112–128. [CrossRef]
17. Laukamp, C. Geological Mapping using Mineral Absorption Feature-Guided Band-Ratios Applied to Prisma Satellite Hyperspectral Level 2D Imagery. In Proceedings of the IGARSS 2022—2022 IEEE International Geoscience and Remote Sensing Symposium, Kuala Lumpur, Malaysia, 17–22 July 2022; pp. 5981–5984. [CrossRef]
18. Marzouki, A.; Dridri, A. Dolomite, quartzite, and sand indices defined for PRISMA hyperspectral data. Application to the Tamlalet inlier (Eastern High Atlas, Morocco). *Adv. Space Res.* **2025**, *75*, 1686–1700. [CrossRef]
19. Cardoso-Fernandes, J.; Santos, D.; Lima, A.; Teodoro, A.C. Assessing the PRISMA Potential for Mineral Exploration to Vector Low-Grade Lithium Deposits. In Proceedings of the IGARSS 2022—2022 IEEE International Geoscience and Remote Sensing Symposium, Kuala Lumpur, Malaysia, 17–22 July 2022; pp. 5985–5988. [CrossRef]
20. Santos, D.; Cardoso-Fernandes, J.; Lima, A.; Teodoro, C. The potential of spectral unmixing method applied to PRISMA hyperspectral images in the identification of Li minerals: An evaluation for prospecting purposes. In *Earth Resources and Environmental Remote Sensing/GIS Applications XIII*; SPIE: Bellingham, WA, USA, 2022; Volume 1226811. [CrossRef]
21. Sorrentino, A.; Chirico, R.; Corrado, F.; Laukamp, C.; Di Martire, D.; Mondillo, N. The application of PRISMA hyperspectral satellite imagery in the delineation of distinct hydrothermal alteration zones in the Chilean Andes: The Marimaca IOCG and the Río Blanco-Los Bronces Cu-Mo porphyry districts. *Ore Geol. Rev.* **2024**, *167*, 105998. [CrossRef]
22. Asadzadeh, S.; Koellner, N.; Chabrillat, S. Detecting rare earth elements using EnMAP hyperspectral satellite data: A case study from Mountain Pass, California. *Sci. Rep.* **2024**, *14*, 20766. [CrossRef] [PubMed]
23. Cormio, C.; Alonso, M.; Cleall, P.; Heuss-Assbichler, S.; Guglietta, D.; Sinnett, D.; Szabo, K.; Zibret, G.; Carvalho, T.; Kral, U.; et al. Site-specific dataset of mining and metallurgical residues for resource management. *Data Brief* **2024**, *54*, 1104811060. [CrossRef] [PubMed]

24. Chen, Q.; Cai, D.; Xia, J.; Zeng, M.; Yang, H.; Zhang, R.; He, Y.; Zhang, X.; Chen, Y.; Xu, X.; et al. Remote sensing identification of hydrothermal alteration minerals in the Duobuza porphyry copper mining area in Tibet using WorldView-3 and GF-5 data: The impact of spatial and spectral resolution. *Ore Geol. Rev.* **2025**, *180*, 106573. [CrossRef]
25. Cogliati, S.; Sarti, F.; Chiarantini, L.; Cosi, M.; Lorusso, R.; Lopinto, E.; Miglietta, F.; Genesio, L.; Guanter, L.; Damm, A.; et al. The PRISMA imaging spectroscopy mission: Overview and first performance analysis. *Remote Sens. Environ.* **2021**, *262*, 112499–112515. [CrossRef]
26. Lööw, J.; Johansson, J. Eight Conditions That Will Change Mining Work in Mining 4.0. *Mining* **2024**, *4*, 904–912. [CrossRef]
27. Guglietta, D.; Conte, A.M.; Paciucci, M.; Passeri, D.; Trapasso, F.; Salvatori, R. Mining Residues Characterization and Sentinel-2A Mapping for the Valorization and Efficient Resource Use by Multidisciplinary Strategy. *Minerals* **2022**, *12*, 617–631. [CrossRef]
28. Chopin, F.; Corsini, M.; Schulmann, K.; El Houicha, M.; Ghienne, J.-F.; Edel, J.-B. Tectonic evolution of the Rehamna metamorphic dome (Morocco) in the context of the Alleghanian-Variscan orogeny. *Tectonics* **2014**, *33*, 1154–1177. [CrossRef]
29. Wernert, P.; Schulmann, K.; Chopin, F.; Stipska, P.; Bosch, D.; El Houicha, M. Tectonometamorphic evolution of an intracontinental orogeny inferred from *P–T–t–d* paths of the metapelites from the Rehamna massif (Morocco). *J. Metamorph. Geol.* **2016**, *34*, 917–940. [CrossRef]
30. Benyas, K.; Aarab, A.; Lakhloufi, A.; Qarbous, A.; Manar, A.; Amar, M.; Idrissi, A.; Elmimouni, M. Contribution of the Airborne Magnetic Field to the Structural Study of the Variscan Granitoid of Rehamna, Morocco. *Iraqi Geol. J.* **2022**, *55*, 21–39. [CrossRef]
31. Dadi, B.; Ouchchen, M.; Faik, F.; Boutaleb, S.; El Azzab, D.; Mamouch, Y.; Achkouch, L.; Bajadi, A.; Abia, E.; Sadeghi, B. Hydrothermal fluid pathways and mineralization potential in the High Atlas Massif (Morocco) using fuzzy logic and multifractal modelling. *Ore Geol. Rev.* **2024**, *175*, 106401–106422. [CrossRef]
32. Maponga, O.; Maxwell, P. The Fall and Rise of African Mining. *Miner. Energy Raw Mat. Rep.* **2001**, *16*, 9–27. [CrossRef]
33. Foose, M.P.; Rossman, D.L. *Geologic Report and Recommendations for the Cobalt Mission to Morocco*; USGS: Reston, VA, USA, 1982. Available online: https://pubs.usgs.gov/of/1982/0618/report.pdf (accessed on 16 May 2025).
34. Corsini, M.; Cornée, J.-J.; Muller, J.; Vauchez, A. *Cisaillement Ductile Synmétamorphe Et Déplacement Tangentiel Vers Le SW Dans Les Rehamna (Maroc Hercynien)*; Comptes Rendus de l'Académie des Sciences: Paris, France, 1988.
35. Hœpffner, C.; Soulaimani, A.; Piqué, A. The Moroccan Hercynides. *J. Afr. Earth Sci.* **2005**, *43*, 144–165. [CrossRef]
36. Clark, R.N.; King, T.V.V.; Klejwa, M.; Swayze, G.A.; Vergo, N. High spectral resolution reflectance spectroscopy of minerals. *J. Geophys. Res.* **1990**, *95*, 12653–12680. [CrossRef]
37. Farmer, V.C. *The Infrared Spectra of Minerals*; Mineralogical Society: London, UK, 1974; pp. 1–539.
38. Hunt, G.R. Spectral signatures of particulate minerals in the visible and near infrared. *Geophysics* **1977**, *42*, 501–513. [CrossRef]
39. Clark, R.N. Spectroscopy of Rocks and Minerals, and Principles of Spectroscopy. In *Remote Sensing for the Earth Sciences: Manual of Remote Sensing*, 3rd ed.; Rencz, A.M., Ed.; Wiley: New York, NY, USA, 1999.
40. Swayze, G.A.; Clark, R.N.; Goetz, A.F.; Livo, K.E.; Breit, G.N.; Kruse, F.A.; Sutley, S.J.; Snee, L.W.; Lowers, H.A.; Post, J.L.; et al. Mapping Advanced Argillic Alteration at Cuprite, Nevada, Using Imaging Spectroscopy. *Econ. Geol.* **2014**, *109*, 1179–1221. [CrossRef]
41. Kokaly, R.F.; Clark, R.N.; Swayze, G.A.; Livo, K.E.; Hoefen, T.M.; Pearson, N.C.; Wise, R.A.; Benzel, W.M.; Lowers, H.A.; Driscoll, R.L.; et al. *USGS Spectral Library Version 7*; U.S. Geological Survey Data Series 1035; USGS: Reston, VA, USA, 2017; pp. 1–61. [CrossRef]
42. Grove, C.I.; Hook, S.J.; Paylor, E.D. Laboratory reflectance spectra for 160 minerals 0.4–2.5 micrometers. In *Report of Jet Propulsion Laboratory Publication*; Jet Propulsion Laboratory: Pasadena, CA, USA, 1992.
43. ASI | Agenzia Spaziale Italiana. Available online: https://www.asi.it/en/#divEarth (accessed on 14 October 2024).
44. Kruse, F.A.; Lefkoff, A.B.; Boardman, J.B.; Heidebrecht, K.B.; Shapiro, A.T.; Barloon, P.J.; Goetz, A.F.H. The Spectral Image Processing System (SIPS)—Interactive Visualization and Analysis of Imaging spectrometer Data. *Remote Sens. Environ.* **1993**, *44*, 145–163. [CrossRef]
45. Boardman, J.W. Inversion of imaging spectrometry data using singular value decomposition. In Proceedings of the IGARSS'89, 12th Canadian Symposium on Remote Sensing, Vancouver, BC, Canada, 10–14 July 1989; Volume 4, pp. 2069–2072.
46. Fultz, B.; Howe, J. Diffraction and the X-Ray Powder Diffractometer. In *Transmission Electron Microscopy and Diffractometry of Materials. Graduate Texts in Physics*, 4th ed.; Springer: Berlin/Heidelberg, Germany, 2013; pp. 1–57. [CrossRef]
47. Heiri, O.; Lotter, A.F.; Lemcke, G. Loss on ignition as a method for estimating organic and carbonate content in sediments: Reproducibility and comparability of results. *J. Paleolimnol.* **2001**, *25*, 101–110. [CrossRef]
48. Ali, A.; Zhang, N.; Santos, R.M. Mineral Characterization Using Scanning Electron Microscopy (SEM): A Review of the Fundamentals, Advancements, and Research Directions. *Appl. Sci.* **2023**, *13*, 12600. [CrossRef]
49. Harmon, R.S.; Senesi, G.S. Laser–induced breakdown spectroscopy—A geochemical tool for the 21st century. *Appl. Geochem.* **2021**, *128*, 104929. [CrossRef]

50. Senesi, G.S.; De Pascale, O.; Mattiello, S.; Moggi Cecchi, V.; Ibhi, A.; Ouknine, L.; Nachit, H. Recent Advances in the Compositional and Mapping Analysis of Iron Meteorites Using a Handheld Laser-Induced Breakdown Spectroscopy Instrument. *Geostand. Geoanal. Res.* **2024**, *48*, 837–862. [CrossRef]
51. Ren, J.; Zabalza, J.; Marshall, S.; Zheng, J. Effective Feature Extraction and Data Reduction in Remote Sensing Using Hyperspectral Imaging. *IEEE Signal Process. Mag.* **2014**, *31*, 149–154. [CrossRef]
52. Schowengerdt, R.A. *Remote Sensing: Models and Methods for Image Processing*, 3rd ed.; Academic Press: Orlando, FL, USA, 2007.
53. Meyer, J.M.; Kokaly, R.F.; Holley, E. Hyperspectral remote sensing of white mica: A review of imaging and point-based spectrometer studies for mineral resources, with spectrometer design considerations. *Remote Sens. Environ.* **2022**, *275*, 1113000. [CrossRef]
54. Cloutier, J.; Piercey, S.J.; Huntington, J. Mineralogy, Mineral Chemistry and SWIR Spectral Reflectance of Chlorite and White Mica. *Minerals* **2021**, *11*, 471–488. [CrossRef]